111 (2023) 204919

Contents lists available at ScienceDirect

Gas Science and Engineering

journal homepage: www.journals.elsevier.com/gas-science-and-engineering

Amplitude variation with angle and azimuth inversion to estimate fracture properties in shale-gas reservoirs

Guangtan Huang [a], Jing Ba [b,*], Davide Gei [c], José M. Carcione [c]

[a] State Key Laboratory of Geomechanics and Geotechnical Engineering, Institute of Rock and Soil Mechanics, Chinese Academy of Sciences, Wuhan, Hubei Province, 430071, China

[b] School of Earth Sciences and Engineering, Hohai University, Nanjing 211100, China

[c] National Institute of Oceanography and Applied Geophysics – OGS, Trieste, Italy

ARTICLE INFO

Keywords:
Amplitude variation with angle and azimuth (AVAZ)
Decoupling
Aspect ratio
Fractures
Saturating fluid

ABSTRACT

Seismic amplitude variation with angle and azimuth inversion is an effective tool for estimating subsurface anisotropic properties from seismic data. Generally, existing methods are oriented toward obtaining elasticity constants, anisotropic coefficients or fracture weaknesses, which are not direct indicators for the exploration and development of hydrocarbons, unlike fracture parameters. Moreover, the conversion from elastic to fracture parameters is based on models subject to error propagation. To overcome these problems, the fracture weaknesses are formulated as a weighted representation of fracture density and aspect ratio and fluid properties. Then, an inversion method is proposed that incorporates the fracture aspect ratio as a spatial variable, which can be applied to estimate water saturation and permeability. Compared with the conventional methods, our approach yields more geological information, as shown by an application to real data.

1. Introduction

Fractures are primary storage and transport pathways of fluids in carbonates, tight sandstones and shale reservoirs (Crampin, 1984; Hsu and Schoenberg, 1993; Bakulin et al., 2000a,b; Oh and Alkhalifah, 2016; Chen et al., 2021; Yang and Liu, 2021). Seismic wave propagation in reservoirs is often characterized by significant velocity anisotropy when aligned fractures are present (Thomsen, 1986). Rocks containing sub-vertical fractures can be assumed to be transversely isotropic with a horizontal symmetry axis (HTI), and their amplitude variation with angle and azimuth (AVAZ) characteristics provide important information to estimate the fracture geometrical properties. This is facilitated by the availability of wide azimuth seismic data.

Seismic inversion is a common practice to obtain the subsurface properties by minimizing the error between observed and synthetic data, subject to certain constraints (Sen and Roy, 2003). To this purpose, a realistic seismic modeling is required (e.g., Carcione and Picotti (2012), Carcione et al. (2012, 2013)). Schoenberg and Protazio (1990) extended the classical Zoeppritz equation to obtain the reflection coefficient in anisotropic media based on Thomsen anisotropy parameters, but the method was not used in inversion algorithms due to its nonlinearity. Based on the assumption of weak anisotropy, Rüger (1997, 1998, 2002) derived a linear approximation of the P-P wave amplitude variation with incidence angle (AVA) for VTI and HTI media (vertical and horizontal symmetry axes, respectively). Subsequently, Shaw and Sen (2004, 2006)) used a scattering theory to derive linear approximations of the P-P and P-SV reflection coefficients for weakly anisotropic HTI media, and transversely isotropic media with a tilted symmetry axis (TTI) as a function of the incidence and azimuth angles, which contributed to the development of the AVAZ seismic inversion theory. Based on the assumption of weak anisotropy, Jin and Stovas (2020) derived reflection and transmission coefficients for qP, qSV and qSH waves.

AVAZ inversion is based on azimuthal seismic gathers as data. Bachrach et al. (2009) introduced a fracture characterization method by using an AVAZ attribute. Based on the Gurevich quasi-static equivalent medium theory, Xue et al. (2017) proposed a generalized fracture weakness to characterize the properties of fluid-saturated fractures. Moreover, AVAZ inversion of fracture weakness was implemented by using a Bayesian framework. Chen et al. (2018) derived approximate P-P and P-SV wave reflection coefficients for weakly anisotropic viscoelastic HTI media, and performed seismic inversion including wave attenuation. Pan et al. (2018) derived an approximation for the P-P wave reflection coefficient based on fracture weakness and performed an AVAZ inversion. Qin et al. (2021) considered TTI media and a characterization based on fracture weakness and an inversion method for tilted fractured strata.

* Corresponding author.
E-mail address: jba@hhu.edu.cn (J. Ba).

https://doi.org/10.1016/j.jgsce.2023.204919
Received 30 June 2022; Received in revised form 6 October 2022; Accepted 5 February 2023
Available online 15 February 2023

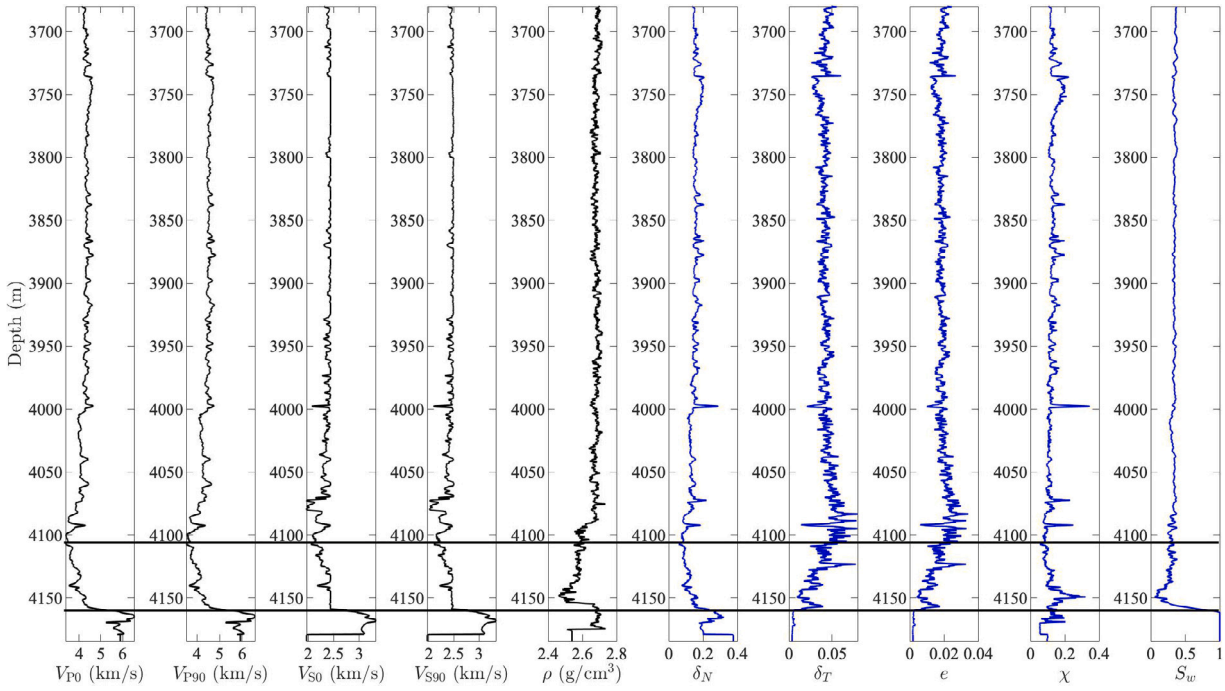

Fig. 1. Well-log data, including the measured P- and S-wave velocities V_{P0}, V_{P90}, V_{S0}, V_{S90}, bulk density ρ, and estimated fracture weaknesses δ_N and δ_T, fracture density e, fracture aspect ratio χ, and water saturation S_w. The profiles between the two black lines indicate the fractured reservoir.

Table 1
List of symbols.

λ, μ	Lamé parameters	$\mathbf{C}$	Stiffness matrix
K	Bulk modulus	M	P-wave modulus
E	Young modulus	ν	Poisson ratio
c	Stiffness component	ρ	Density
c_b	Stiffness component of the host medium	ρ_b	Density of the host medium
α	P-wave velocity	β	S-wave velocity
R_{PP}	P-P wave reflection coefficient	R_{PP}^{iso}	Isotropic part of R_{PP}
R_{PP}^{ani}	Anisotropic part of R_{PP}	$\mathbf{t}$	Wavevector
θ	Incidence angle	ϕ	Azimuthal angle
ζ	μ/M	γ	λ/M
e	Fracture density	χ	Fracture aspect ratio
Δ	Perturbation	δ_N, δ_T	Fracture weakness
S_w	Water saturation	$\mathbf{p}$	Slowness vector
$\mathbf{S}$	Seismic data	$\mathbf{W}$	Wavelet matrix

The aforementioned methods mainly focus on estimating the fracture weaknesses, which are affected by the fracture geometry and filling materials (Chen et al., 2014, 2015, 2017; Pan et al., 2019a,b, 2021; Li et al., 2022). A quantitative estimation of such fracture properties (e.g., fracture density, aspect ratio and saturation) is meaningful for the production and development of hydrocarbon reservoirs. To address complex fracture structures, such as the spatial variation of the fracture aspect ratio, an AVAZ inversion is proposed to estimate the fracture density, aspect ratio and saturation.

First, the fracture weaknesses are decoupled by combining the coin-shaped fracture model (Hudson, 1981), linear-slip model (Schoenberg and Sayers, 1995), and using Wood's equation (Domenico, 1976). Then, an approximate reflection coefficient is obtained, as a function of fracture density, aspect ratio and saturation. Further, the forward operator is introduced into the AVAZ inversion. The method updates those properties during the optimization process, aiming at improving the accuracy of the inversion results. A sensitivity analysis is performed to evaluate the reliability of the parameter estimation and finally the proposed method is applied to field data. To aid the comprehension of the text and equations, Table 1 shows the list of symbols.

2. Methodology

2.1. Fracture-fluid decoupling

The background is assumed to be a homogeneous medium with porosity due to fractures only. The media above and below the interface are both HTI with the same fracture azimuth, i.e., they have the same horizontal symmetry axis.

Based on the Hudson (1981) model and the linear slip model of Schoenberg and Sayers (1995), the fracture weaknesses of a HTI media are

$$\delta_N = \frac{4e}{3\zeta_b\left(1-\zeta_b\right)\left[1+\frac{1}{\pi\left(1-\zeta_b\right)}\frac{K'}{\mu_b\chi}\right]} = \frac{4e}{3\zeta_b}\cdot\frac{1}{1-\zeta_b+\frac{K'}{\pi\mu_b\chi}}, \tag{1}$$

$$\delta_T = \frac{16e}{3\left(3-2\zeta_b\right)}, \tag{2}$$

where K' is the bulk modulus of the fluid saturating the fractures, $\zeta_b = \mu_b/M_b$, $M_b = \lambda_b + 2\mu_b$, with λ_b and μ_b the Lamé parameters of the host media, and e and χ are the fracture density and aspect ratio, respectively. ζ_b is assumed constant, related to the host matrix can be

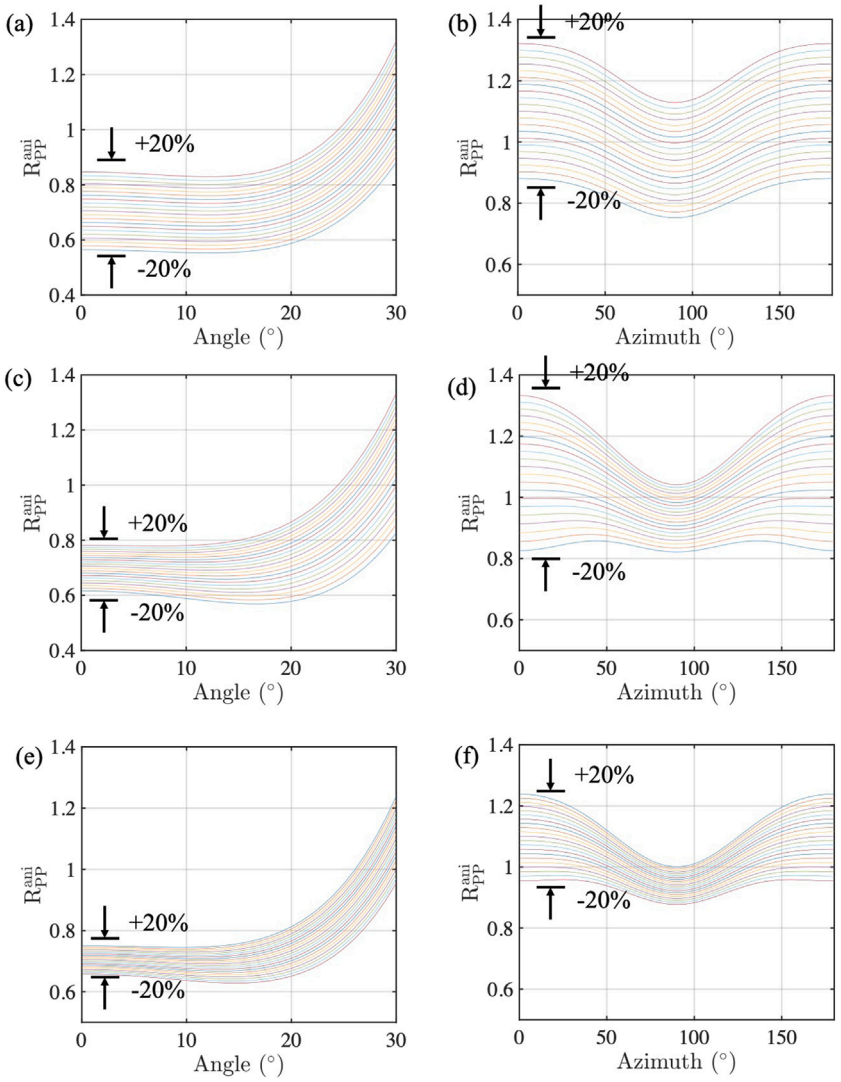

Fig. 2. Effects on the AVA and AVAZ reflection coefficients induced by the perturbation of (a, b) fracture density, (c, d) fracture aspect ratio, (e, f) water saturation. (a), (c), and (e) correspond to the AVA at 0° azimuth angle, and (b), (d), and (f) to the AVAZ at 30° incidence angle.

obtained by a conventional AVA inversion. The fracture fluid indicator is defined as

$$F_c = 1 - \zeta_b + \frac{K'}{\pi \mu_b \chi}, \tag{3}$$

such that

$$\delta_N = \frac{4e}{3\zeta_b} \cdot \frac{1}{F_c}. \tag{4}$$

The perturbations of the fracture weaknesses related to the upper and lower media can be obtained in a differential form, to give

$$\Delta\delta_N = \delta_N^{\text{lower}} - \delta_N^{\text{upper}} \approx d(\delta_N) = d\left(\frac{4e}{3\zeta_b} \cdot \frac{1}{F_c}\right) = \delta_N \frac{\Delta e}{e} - \delta_N \frac{\Delta F_c}{F_c}, \tag{5}$$

$$\Delta\delta_T = \delta_T^{\text{lower}} - \delta_T^{\text{upper}} \approx d(\delta_T) = d\left(\frac{16e}{3(3-2\zeta_b)}\right) = \delta_T \frac{\Delta e}{e}. \tag{6}$$

Defining the compressibility $Z = \frac{1}{K}$, we have

$$\begin{aligned}\Delta F_c &= \Delta\left(1 - \zeta_b + \frac{1}{\pi \mu_b Z' \chi}\right) = \frac{1}{\pi \mu_b}\left(\frac{1}{Z'^{\text{lower}} \chi^{\text{lower}}} - \frac{1}{Z'^{\text{upper}} \chi^{\text{upper}}}\right) \\ &= (1 - \zeta_b - F_c)\left(\frac{\Delta Z'}{Z'} + \frac{\Delta \chi}{\chi}\right).\end{aligned} \tag{7}$$

Thus

$$\frac{\Delta F_c}{F_c} = \left(\frac{1-\zeta_b}{F_c} - 1\right)\left(\frac{\Delta Z'}{Z} + \frac{\Delta \chi}{\chi}\right). \tag{8}$$

For shale gas reservoirs, the saturating fluids are water and gas. According to Wood's equation,

$$Z' = S_w Z_w + (1 - S_w) Z_g = (Z_w - Z_g) S_w + Z_g, \tag{9}$$

where the subscripts $\{\cdot\}_w$ and $\{\cdot\}_g$ denote the properties of water and gas. Thus

$$\frac{\Delta Z'}{Z'} = \frac{S_w\left(Z_w - Z_g\right)}{Z'} \frac{\Delta S_w}{S_w}. \tag{10}$$

By combining Eqs. (5), (6), (8) and (10), the perturbations of fracture weaknesses are

$$\begin{aligned}\Delta\delta_T &= \delta_T \frac{\Delta e}{e}, \\ \Delta\delta_N &\approx \delta_N \frac{\Delta e}{e} + \delta_N \left(1 - \frac{1-\zeta_b}{F_c}\right)\left[\frac{S_w\left(Z_w - Z_g\right)}{Z'} \frac{\Delta S_w}{S_w} + \frac{\Delta \chi}{\chi}\right] \\ &= k_e \frac{\Delta e}{e} + k_\chi \frac{\Delta \chi}{\chi} + k_{S_w} \frac{\Delta S_w}{S_w},\end{aligned} \tag{11}$$

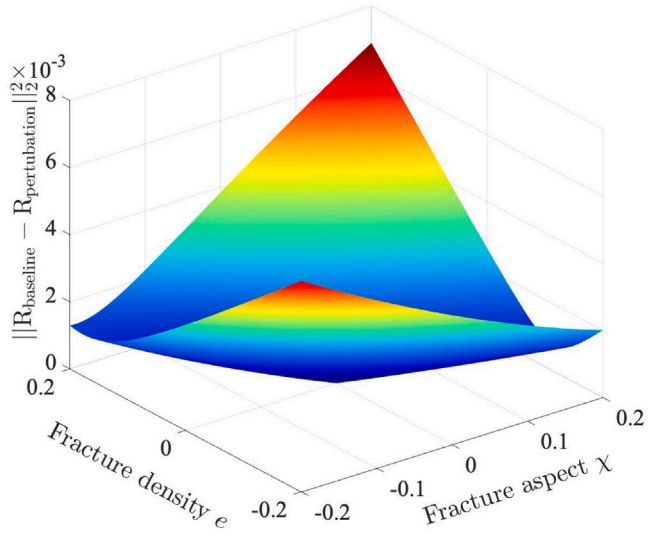

(a)

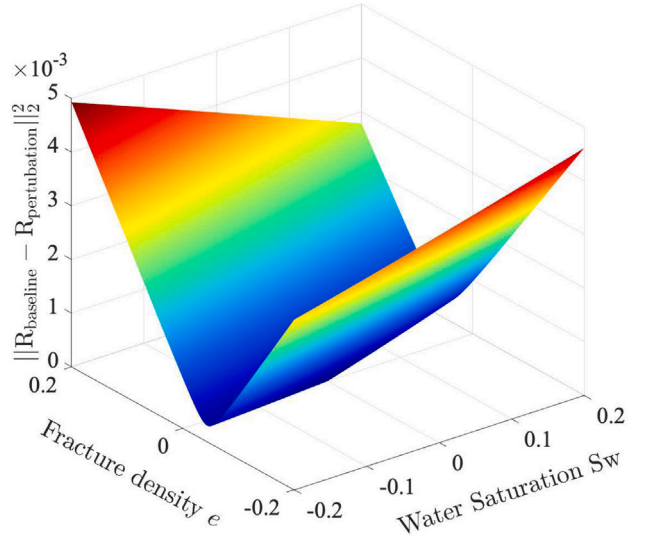

(b)

Fig. 3. The ℓ_2 misfit between the baseline and reflection coefficient computed with the perturbed reservoir properties $\|\mathrm{R}_{\text{baseline}} - \mathrm{R}_{\text{perturbation}}\|_2^2$.

where

$$k_e = \delta_N, \quad k_\chi = \delta_N \left(1 - \frac{1-\zeta_b}{F_c}\right), \quad k_{S_w} = \delta_N \left(1 - \frac{1-\zeta_b}{F_c}\right) \frac{S_w \left(Z_w - Z_g\right)}{Z'}. \tag{12}$$

2.2. Forward operator

According to Shaw and Sen (2004, 2006), the linearized P-P wave reflection coefficient in weakly anisotropic media is

$$\mathrm{R_{PP}} = \frac{1}{4\rho_b \cos^2\theta} \left(\Delta\rho\xi + \Delta c_{IJ}\eta_{IJ}\right), \quad (I, J = 1, 2, \ldots, 6), \tag{13}$$

where ρ_b is the host density, with $\Delta\rho$ its perturbation, Δc_{IJ} are the stiffness perturbations due to anisotropy, θ is the incidence angle, and ξ and η_{IJ} are defined in Appendix A.

The stiffness matrix of the resulting HTI media is

$$\mathbf{C} = \mathbf{C}_b + \Delta\mathbf{C} = \begin{bmatrix} M_b & \lambda_b & \lambda_b & 0 & 0 & 0 \\ \lambda_b & M_b & \lambda_b & 0 & 0 & 0 \\ \lambda_b & \lambda_b & M_b & 0 & 0 & 0 \\ 0 & 0 & 0 & \mu_b & 0 & 0 \\ 0 & 0 & 0 & 0 & \mu_b & 0 \\ 0 & 0 & 0 & 0 & 0 & \mu_b \end{bmatrix} - \begin{bmatrix} M_b\Delta\delta_N & \lambda_b\Delta\delta_N & \lambda_b\Delta\delta_N & 0 & 0 & 0 \\ \lambda_b\Delta\delta_N & \frac{\lambda_b^2}{M_b}\Delta\delta_N & \frac{\lambda_b^2}{M_b}\Delta\delta_N & 0 & 0 & 0 \\ \lambda_b\Delta\delta_N & \frac{\lambda_b^2}{M_b}\Delta\delta_N & \frac{\lambda_b^2}{M_b}\Delta\delta_N & 0 & 0 & 0 \\ 0 & 0 & 0 & 0 & 0 & 0 \\ 0 & 0 & 0 & 0 & \mu_b\Delta\delta_T & 0 \\ 0 & 0 & 0 & 0 & 0 & \mu_b\Delta\delta_T \end{bmatrix}, \tag{14}$$

where the first matrix corresponds to the isotropic background medium. Then, a simplified form is

$$\mathrm{R_{PP}}(\theta,\phi) = a_M(\theta)\frac{\Delta M_b}{M_b} + a_\mu(\theta)\frac{\Delta\mu_b}{\mu_b} + a_\rho(\theta)\frac{\Delta\rho_b}{\rho_b} + a_{\delta_N}(\theta,\phi)\Delta\delta_N + a_{\delta_T}(\theta,\phi)\Delta\delta_T, \tag{15}$$

where

$$\begin{aligned} a_M &= \frac{1}{4\cos^2\theta}, \quad a_\mu = -2\zeta_b \sin^2\theta, \quad a_\rho = \frac{1}{2} - \frac{1}{4\cos^2\theta}, \\ a_{\delta_N} &= \frac{1}{4\cos^2\theta}\left[2\zeta_b(\sin^2\theta\sin^2\phi + \cos^2\theta) - 1\right]^2, \\ a_{\delta_T} &= \zeta_b \sin^2\theta\cos^2\phi(1 - \tan^2\theta\sin^2\phi), \end{aligned} \tag{16}$$

and substituting (11) into (15),

$$\mathrm{R_{PP}}(\theta,\phi) = a_M(\theta)\frac{\Delta M_b}{M_b} + a_\mu(\theta)\frac{\Delta\mu_b}{\mu_b} + a_\rho(\theta)\frac{\Delta\rho_b}{\rho_b} + a_e(\theta,\phi)\frac{\Delta e}{e} + a_\chi(\theta,\phi)\frac{\Delta\chi}{\chi} + a_{S_w}(\theta,\phi)\frac{\Delta S_w}{S_w}, \tag{17}$$

in terms of fracture density, aspect ratio and saturation, and

$$a_e = a_{\delta_N}k_e + a_{\delta_T}\delta_T, \quad a_\chi = a_{\delta_N}k_\chi, \quad a_{Sw} = a_{\delta_N}k_{Sw}. \tag{18}$$

As shown in Eq. (17), the reflection coefficient can be partitioned into azimuth-independent and azimuth-dependent terms, which correspond to the isotropic and anisotropic parts, respectively.

$$\mathrm{R_{PP}}(\theta,\phi) = \mathrm{R_{PP}^{iso}}(\theta) + \mathrm{R_{PP}^{ani}}(\theta,\phi). \tag{19}$$

2.3. Inversion theory

The azimuthal seismic data can be obtained by convolving the reflectivity with the seismic wavelet. We have

$$\mathbf{S_{PP}}(\theta,\phi) = \mathbf{W}(\theta,\phi)\cdot\mathbf{R_{PP}}(\theta,\phi) + \mathbf{e}, \tag{20}$$

where $\mathbf{W}$ is the seismic-wavelet matrix, $\mathbf{e}$ is the noise vector, the dot denotes a matrix/vector product and

$$\mathbf{R_{PP}}(\theta,\phi) = \begin{bmatrix} \mathrm{R_{PP}}(1,\theta,\phi) \\ \mathrm{R_{PP}}(2,\theta,\phi) \\ \vdots \\ \mathrm{R_{PP}}(i,\theta,\phi) \\ \vdots \\ \mathrm{R_{PP}}(N,\theta,\phi) \end{bmatrix}^T, \tag{21}$$

for N time samples.

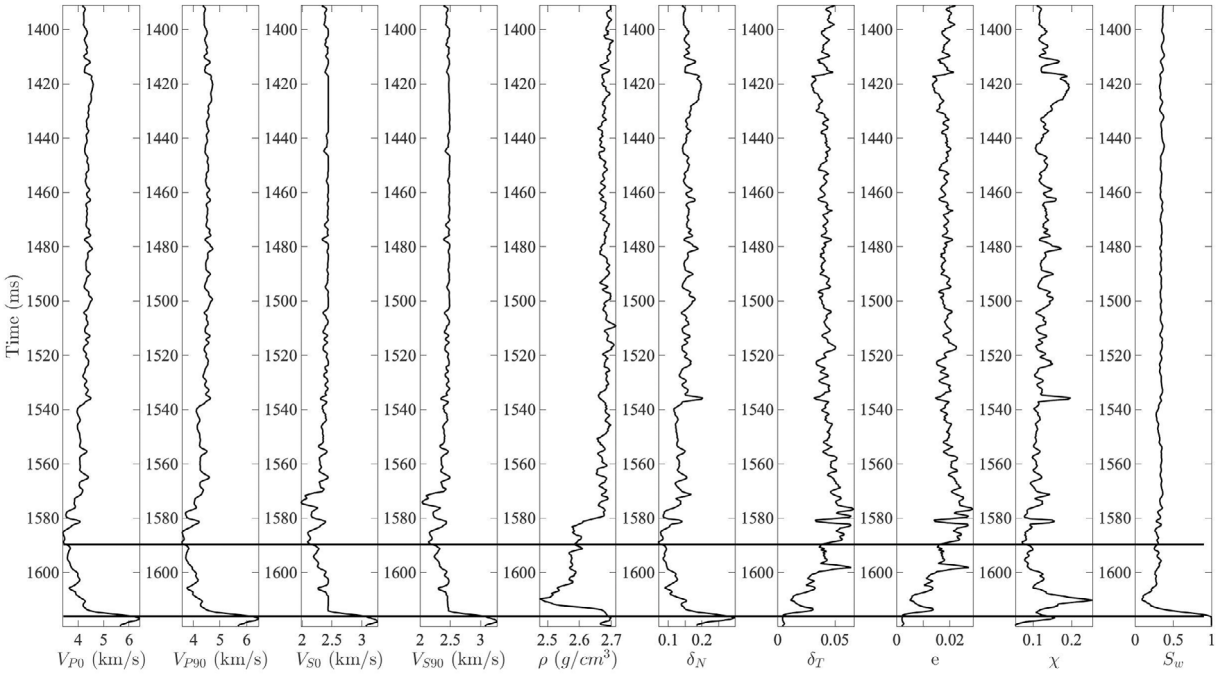

Fig. 4. Well-log data in time domain, including the measured P- and S-wave velocities V_{P0}, V_{P90}, V_{S0}, V_{S90}, bulk density ρ, and estimated fracture weaknesses δ_N and δ_T, fracture density e, fracture aspect ratio χ, and water saturation S_w. The profiles between the two black lines indicate the fractured reservoir.

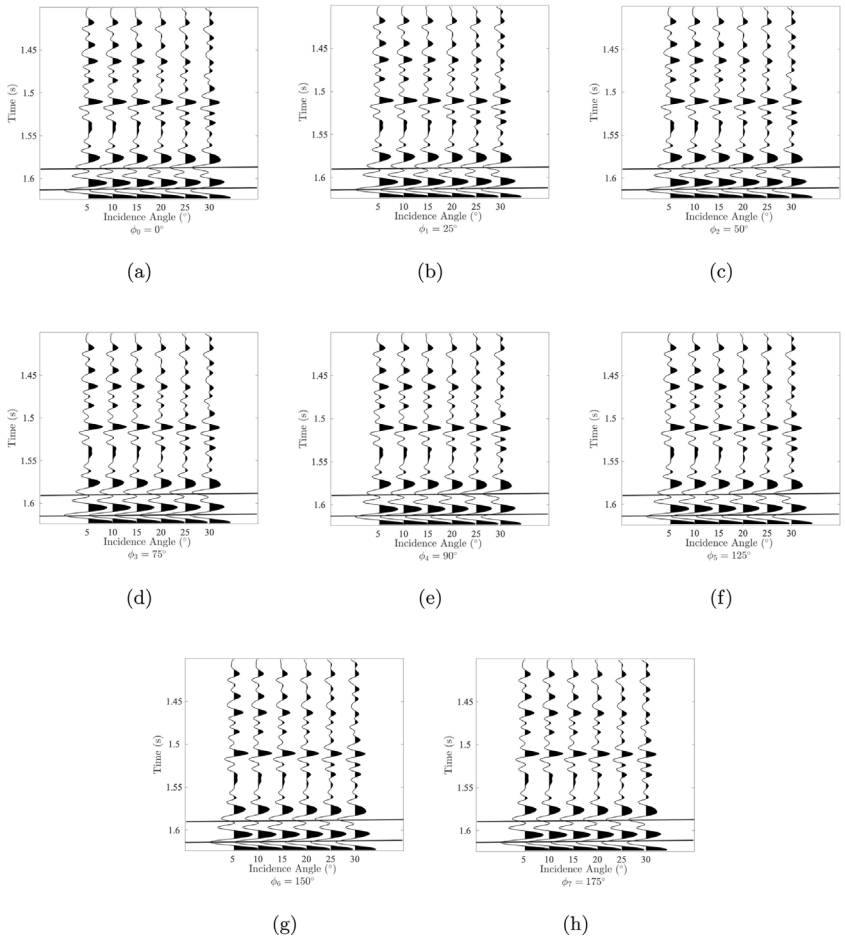

Fig. 5. Simulated azimuthal pre-stack angle gathers by using Eq. (20). The profiles between the two black lines indicate the fractured reservoir.

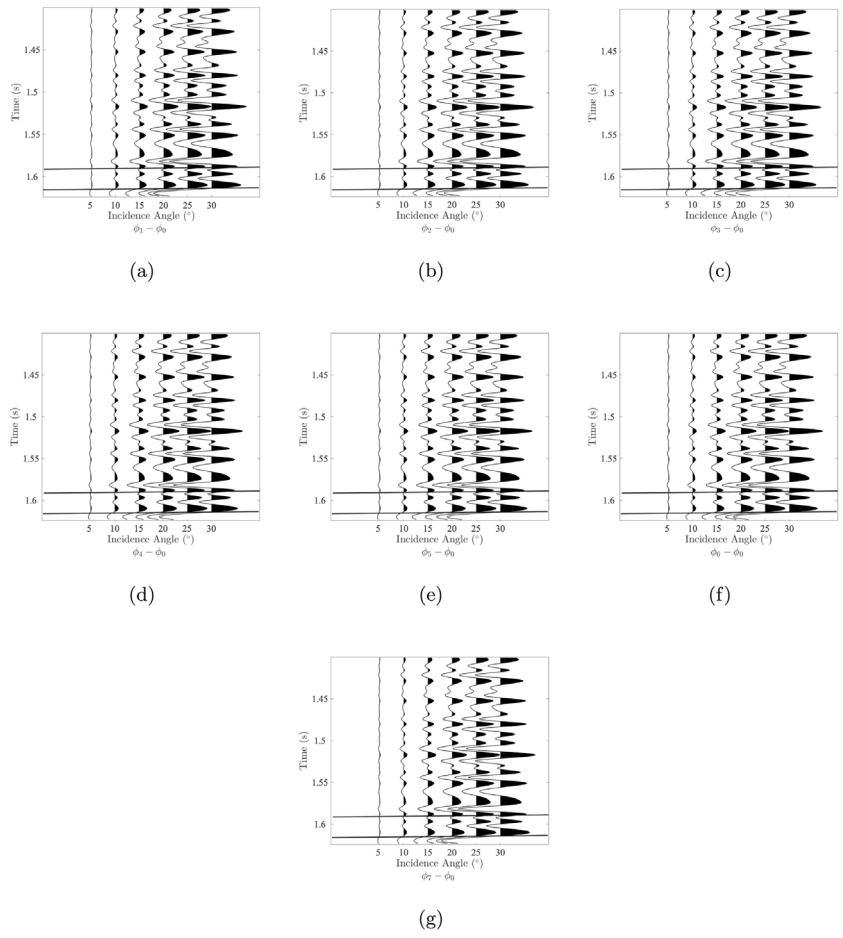

Fig. 6. Residual profiles between 0° and different azimuthal gathers ranging from 25° to 175° with 25° intervals. The profiles between the two black lines indicate the fractured reservoir.

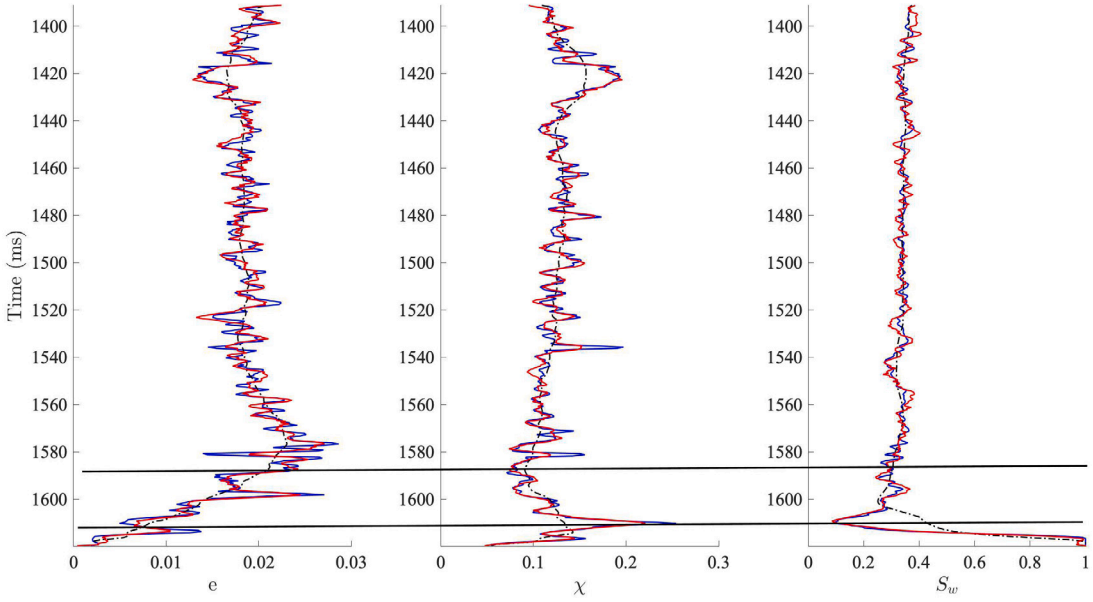

Fig. 7. Inverted fracture density, aspect ratio and water saturation (red dashed line) by using proposed method and the well-log data (blue solid line). The profiles between the two black lines indicate the fractured reservoir.

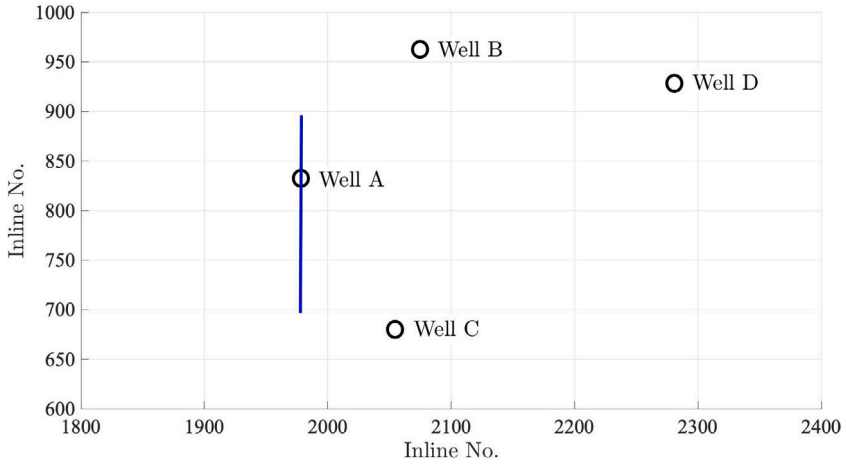

Fig. 8. The distribution of well-log with the target area. The blue solid-dotted line is the inline profile used to test the inversion effects of the field data, and Well A are used for comparison and verification.

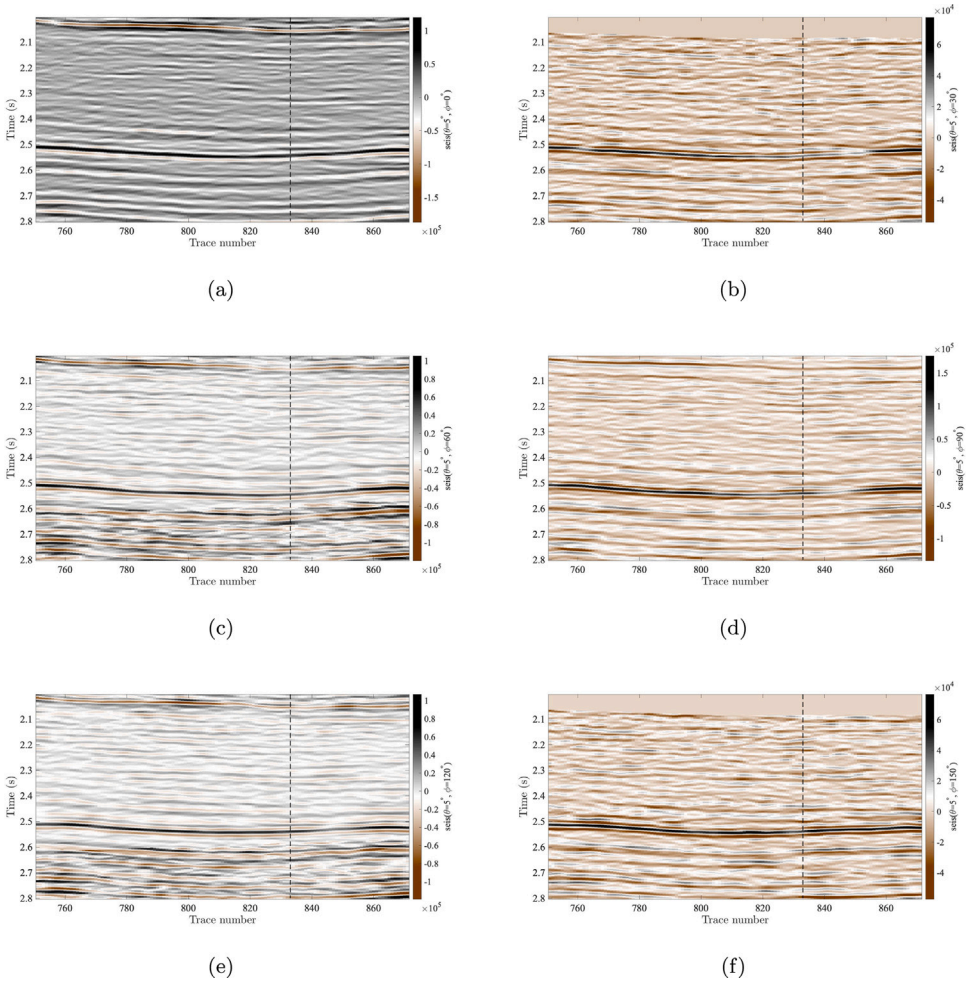

Fig. 9. Near-incidence-angular partial stack seismic profiles at different azimuths ϕ, i.e., (a) 0°, (b) 30°, (c) 60°, (d) 90°, (e) 120°, (f) 150°. The black dashed lines denote the well location.

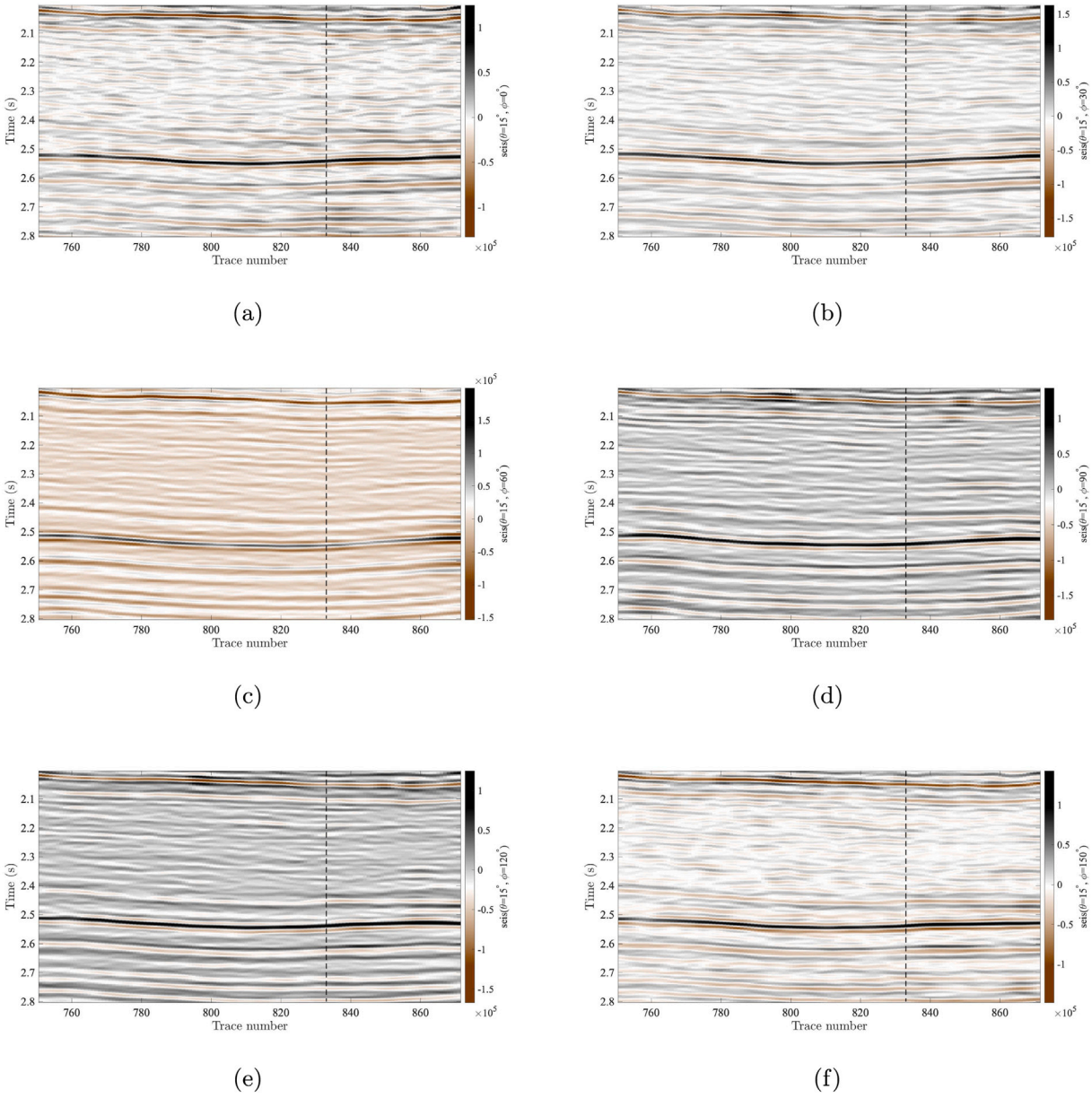

Fig. 10. Mid-incidence-angular partial stack seismic profiles at different azimuths ϕ, i.e., (a) 0°, (b) 30°, (c) 60°, (d) 90°, (e) 120°, (f) 150°. The black dashed lines denote the well location.

The amplitude difference with respect to different azimuths $\Delta\mathbf{S}_{\mathrm{PP}}\left(\theta,\Delta\phi_{ij}\right)$ is

$$\begin{aligned}\Delta\mathbf{S}_{\mathrm{PP}}\left(\theta,\Delta\phi_{ij}\right)&=\mathbf{S}_{\mathrm{PP}}\left(\theta,\Delta\phi_{i}\right)-\mathbf{S}_{\mathrm{PP}}\left(\theta,\Delta\phi_{j}\right)\\&=\overline{\mathbf{W}}(\theta,\phi_{i},\phi_{j})\cdot\left[\mathbf{R}_{\mathrm{PP}}\left(\theta,\phi_{i}\right)-\mathbf{R}_{\mathrm{PP}}\left(\theta,\phi_{j}\right)\right],\end{aligned}\tag{22}$$

where $\overline{\mathbf{W}}(\theta,\phi_i,\phi_j)$ indicate the average of $\mathbf{W}(\theta,\phi_i)$ and $\mathbf{W}(\theta,\phi_j)$. According to Eqs. (17)–(19), the amplitude difference $\Delta\mathbf{S}_{\mathrm{PP}}\left(\theta,\Delta\phi_{ij}\right)$ can be further separated as

$$\begin{aligned}&\Delta\mathbf{S}_{\mathrm{PP}}\left(\theta,\Delta\phi_{ij}\right)\\&=\overline{\mathbf{W}}\cdot\left[\left(\mathbf{R}_{\mathrm{PP}}^{\mathrm{iso}}\left(\theta\right)+\mathbf{R}_{\mathrm{PP}}^{\mathrm{ani}}\left(\theta,\phi_{i}\right)\right)-\left(\mathbf{R}_{\mathrm{PP}}^{\mathrm{iso}}\left(\theta\right)+\mathbf{R}_{\mathrm{PP}}^{\mathrm{ani}}\left(\theta,\phi_{j}\right)\right)\right]\\&=\overline{\mathbf{W}}\cdot\left[a_{e}\left(\theta,\phi_{i}\right)-a_{e}\left(\theta,\phi_{j}\right)\quad a_{\chi}\left(\theta,\phi_{i}\right)-a_{\chi}\left(\theta,\phi_{j}\right)\quad a_{S_{w}}\left(\theta,\phi_{i}\right)-a_{S_{w}}\left(\theta,\phi_{j}\right)\right]\\&\quad\times\begin{bmatrix}\mathbf{r}_{e}\\\mathbf{r}_{\chi}\\\mathbf{r}_{S_{w}}\end{bmatrix},\end{aligned}\tag{23}$$

where

$$r_e=\frac{\Delta e}{e},\quad r_{\chi}=\frac{\Delta\chi}{\chi},\quad r_{Sw}=\frac{\Delta Sw}{Sw}.\tag{24}$$

The inversion minimizes the differences between observed and synthetic data under certain constraints (Alemie and Sacchi, 2011). The objective function is

$$\mathbf{J}(\mathbf{m})=\|\Delta\mathbf{S}_{\mathrm{PP}}^{\mathrm{obs}}-\Delta\mathbf{S}_{\mathrm{PP}}^{\mathrm{syn}}(\mathbf{m})\|_2^2+(\mathbf{m}-\mathbf{m}_{\mathbf{e}})^{T}\boldsymbol{\Sigma}_{\mathbf{m}}{}^{-1}(\mathbf{m}-\mathbf{m}_{\mathbf{e}})\tag{25}$$

where $\mathbf{S}_{\mathrm{PP}}^{\mathrm{obs}}$ and $\mathbf{S}_{\mathrm{PP}}^{\mathrm{syn}}$ are the observed and synthetic data, $\mathbf{m}=[\mathbf{r}_e,\mathbf{r}_{\chi},\mathbf{r}_{S_w}]^T$ is the vector of sought parameters, $\mathbf{m_e}$ and $\boldsymbol{\Sigma}_{\mathbf{m}}$ are the mean and covariance matrices of these parameters, respectively. The gradient-based method is adopted to minimize the objective function.

3. Sensitivity analysis

A sensitivity analysis is performed to evaluate the reliability of the parameter estimation. The well-log data shown in Fig. 1 is considered,

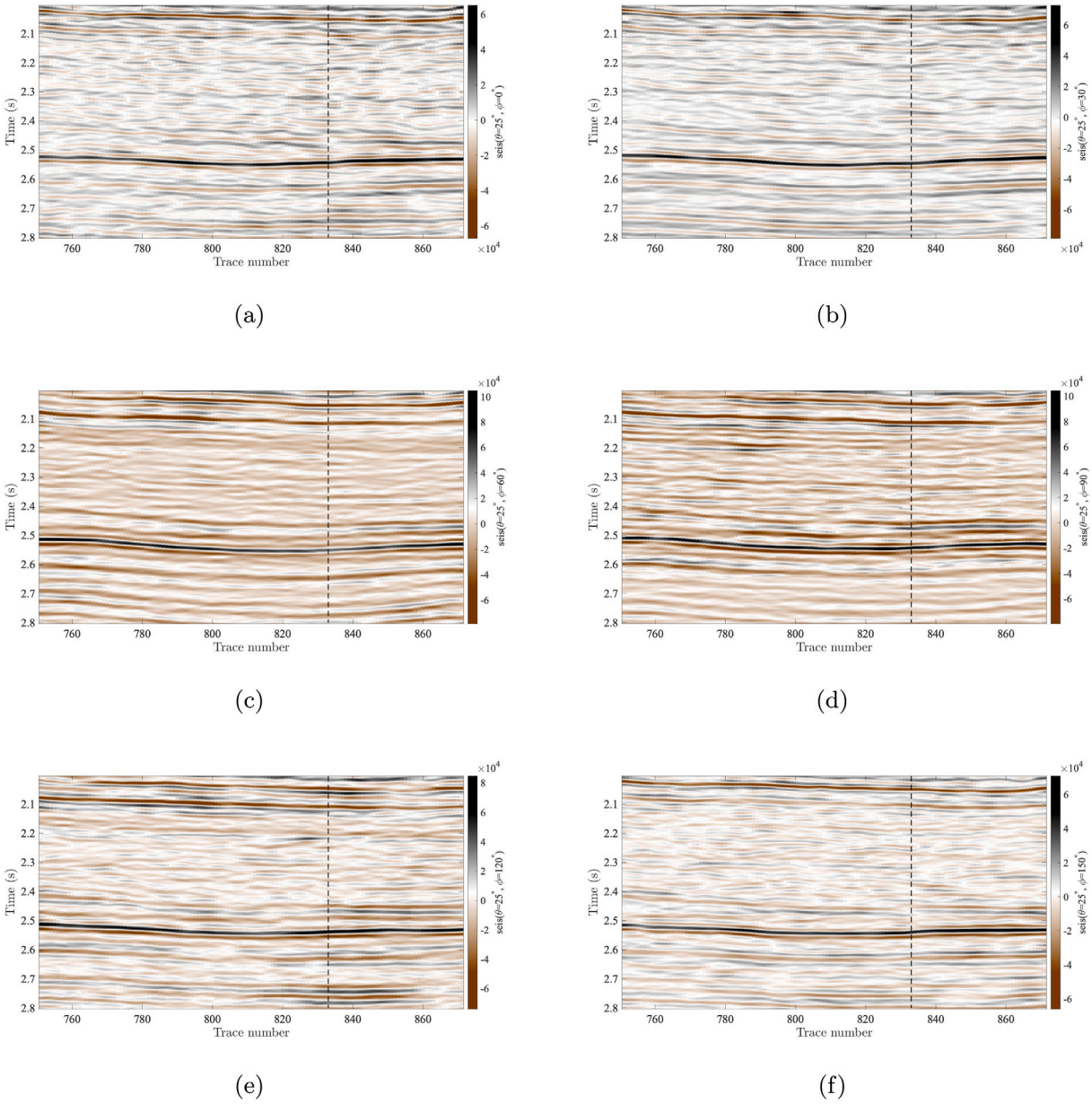

Fig. 11. Far-incidence-angular partial stack seismic profiles at different azimuths ϕ, i.e., (a) 0°, (b) 30°, (c) 60°, (d) 90°, (e) 120°, (f) 150°. The black dashed lines denote the well location.

where the black and blue curves represent the measured and estimated data, respectively. V_{P0} and V_{S0} are the P- and S-wave vertical velocities, and V_{P90} and V_{S90} are the P- and S-wave horizontal velocities, respectively,

$$\begin{aligned} c_{33} &= \rho V_{P,0}^2 \quad , \quad c_{66} = \rho V_{S,0}^2, \\ c_{11} &= \rho V_{P,90}^2 \quad , \quad c_{44} = \rho V_{S,90}^2, \end{aligned} \tag{26}$$

(Zhang et al. 2019). The fracture weakness can be estimated from the following relations

$$\begin{aligned} \frac{c_{11} - c_{33}}{2c_{33}} &= -2\zeta_b(1-\zeta_b)\delta_N, \\ \frac{c_{66} - c_{44}}{2c_{44}} &= -2\zeta_b\left[(1-2\zeta_b)\delta_N + \delta_T\right]. \end{aligned} \tag{27}$$

Then, using Eqs. (1), (2) and (9), we estimate the fracture density and aspect ratio. The interval between the two black horizontal lines indicates a fractured formation (the target layer) overlaid by a mudstone layer.

Here we mainly focus on the contributions of the fracture density e, aspect ratio χ, and water saturation S_w to the seismic response. The sensitivity analysis is performed by varying the properties of the target layer (−20%–20%). The parameters to obtain the reflection coefficients, according to Eq. (17), are the average of the values of overlying strata (ranges from 4050 to 4105) and reservoir (ranges from 4105 to 4160).

Figs. 2a and 2b show how the fracture density affects the AVA at 0° azimuth, and the AVAZ at 30° incidence angle, respectively. Figures 2c,d and 2e,f show the same for the aspect ratio and water saturation, respectively. The effect of water saturation shows lower sensitivity, and we expect the inversion of fracture density and aspect ratio to be more reliable.

By fixing one of the three parameters, e, χ and S_w, the ℓ_2-norm misfit between the reflection coefficient with and without perturbation can be calculated. The contribution of fracture density and aspect ratio to the misfit is similar as the misfit changes along the diagonal, as

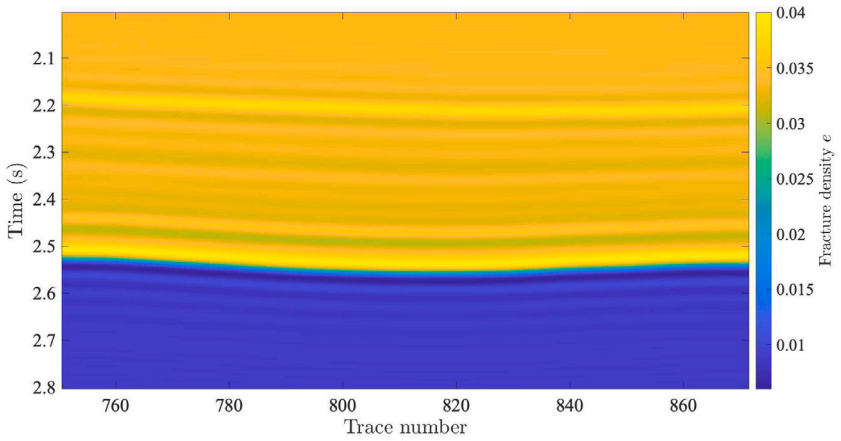

(a)

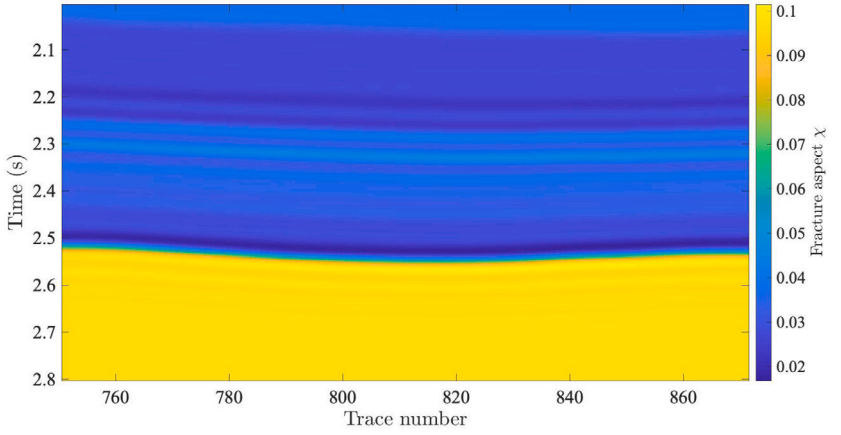

(b)

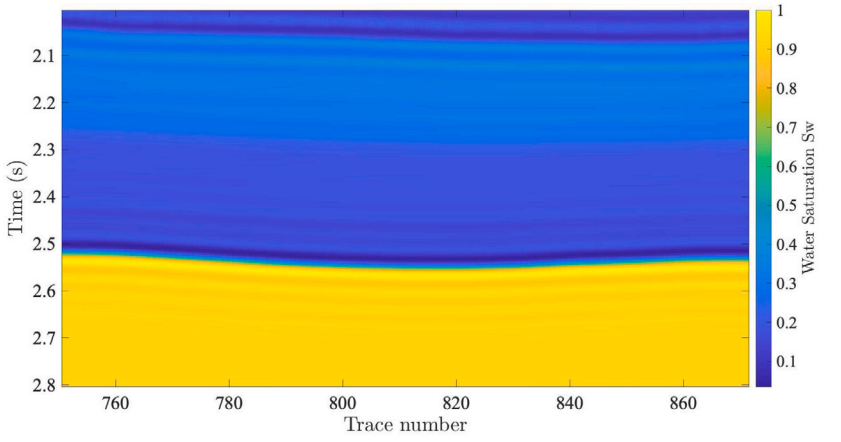

(c)

Fig. 12. Initial model of (a) fracture density, (b) aspect ratio, and (c) water saturation obtained from well-log data interpolation.

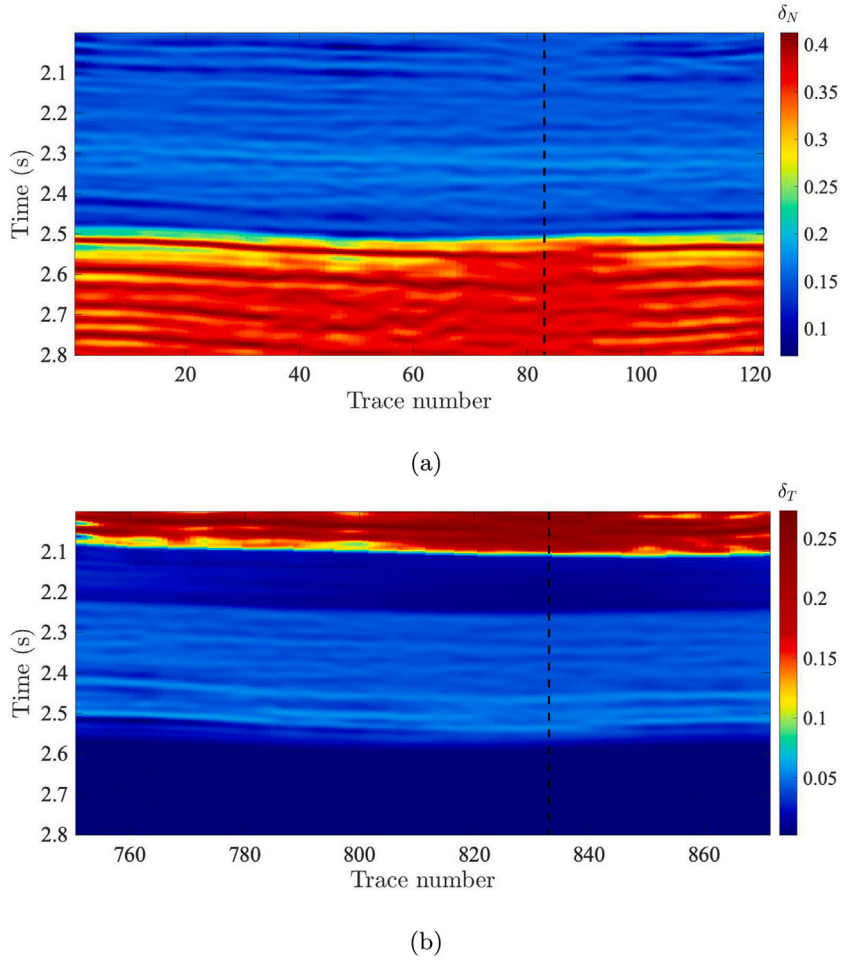

Fig. 13. Inverted fracture weaknesses δ_N and δ_T based on the conventional AVAZ inversion.

shown in Fig. 3a. Instead, the contribution of the fracture density is higher than that of the water saturation (see Fig. 3b).

4. Example

In Fig. 1 we consider well-log data and obtain the fracture-related parameters e, χ and S_w by using the proposed theory. Fig. 4 shows the well-log curves in the time domain by using a seismic-well tie, including the P- and S-wave velocities, density, and the estimated fracture weaknesses δ_N and δ_T.

Firstly, Eq. (20) is adopted to compute the synthetic input data, where the incidence angle ranges from 0° to 30°, and the azimuth angle from 0° to 180°. We consider the following Ricker wavelet with a dominant frequency $f_0 = 30$ Hz and ignore the dependency of wavelets with angle and azimuth

$$w(t) = \left[1 - 2(\pi f_0 t)^2\right] e^{-(\pi f_0 t)^2}. \tag{28}$$

We obtain the azimuthal angle gathers, as shown in Fig. 5, where we observe that the angle gathers hardly vary with azimuth. Such small differences correspond to the contribution of the anisotropy parameters. Fig. 6 shows azimuthal difference angle gathers obtained from the gathers of Fig. 5. It shows that the difference is mainly present at far angles and implies that δ_N and δ_T have a higher sensitivity and contribution to the azimuthal seismic data at mid and far angles.

Fig. 7 shows the fracture parameters by solving Eq. (25), where the solid blue and red lines indicate the real well-log data and inversion results, respectively. Basically, these results are consistent with the true values.

5. Real-data example

5.1. Data description

The inversion is applied to 2-D azimuthal pre-stack seismic data and is validated by comparison to well-log data. The data is acquired from a fractured shale reservoir in south-western China, which include 500 lines with 800 CDPs per line. Conventional well log and anisotropy measurements were performed at 4 wells probing the target area. Fig. 8 shows the distribution of the wells, and the blue solid line indicates the location of the 2-D section, consisting in 120 azimuthal pre-stack seismic gathers. The incidence angle of each gather ranges from 0° to 30° with an increment of 3°, and the azimuth angle ranges from 0° to 180° with an increment of 30°. Well A is drilled at gather 82 (black dashed line in Figs. 9–11) where a shale gas reservoir has been identified between 2.4 and 2.5 s.

5.2. Application

An inversion test is performed with the 2-D pre-stack azimuthal seismic data and is further validated by a comparison between the well-log data and inversion results of borehole-side angle gathers. Figs. 9–11 show the near (0°-10°) -, middle (10°-20°)-, and far (20°-30°) -incidence-angular partial stack seismic profiles at different azimuth angles ϕ, i.e., (a) 0°, (b) 30°, (c) 60°, (d) 90°, (e) 120°, (f) 150°. The initial model is obtained by using well-log data interpolation based on geological structure-oriented constraints (Huang et al., 2020), as shown in Fig. 12. The fracture density and aspect ratio are estimated by using

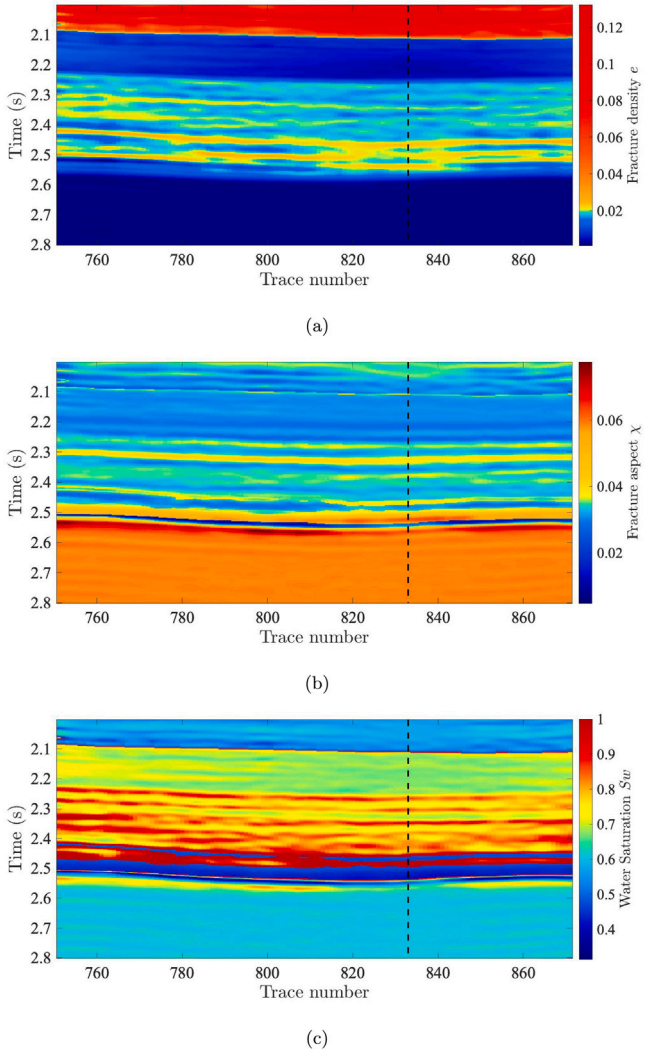

Fig. 14. Inversion results for (a) fracture density, (b) aspect ratio and (b) water saturation by using the proposed method.

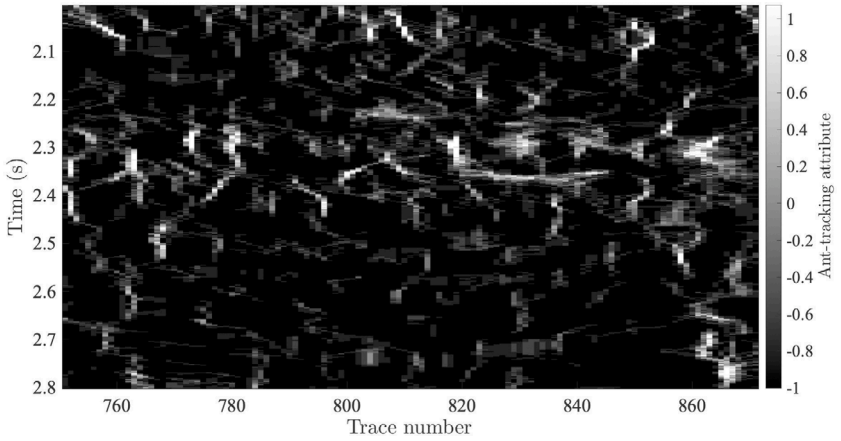

Fig. 15. Fracture-related ant-body attribute by using the ant-tracking algorithm.

well-bore imaging. In the comparison, conventional AVAZ inversion is adopted to extract the fracture properties from the data. The fracture weaknesses δ_N and δ_T, obtained from the linear-slip model, are shown in Fig. 13, where we can see that the fracture weaknesses, δ_T can better discriminate the fractures: in Fig. 13b, the strata above 2.1 s exhibit a high value.

Fig. 14 shows the final inversion results. Compared to the fracture-weakness-based inversion method, the proposed approach provides more information. The fracture density reveals the degree of fracturing,

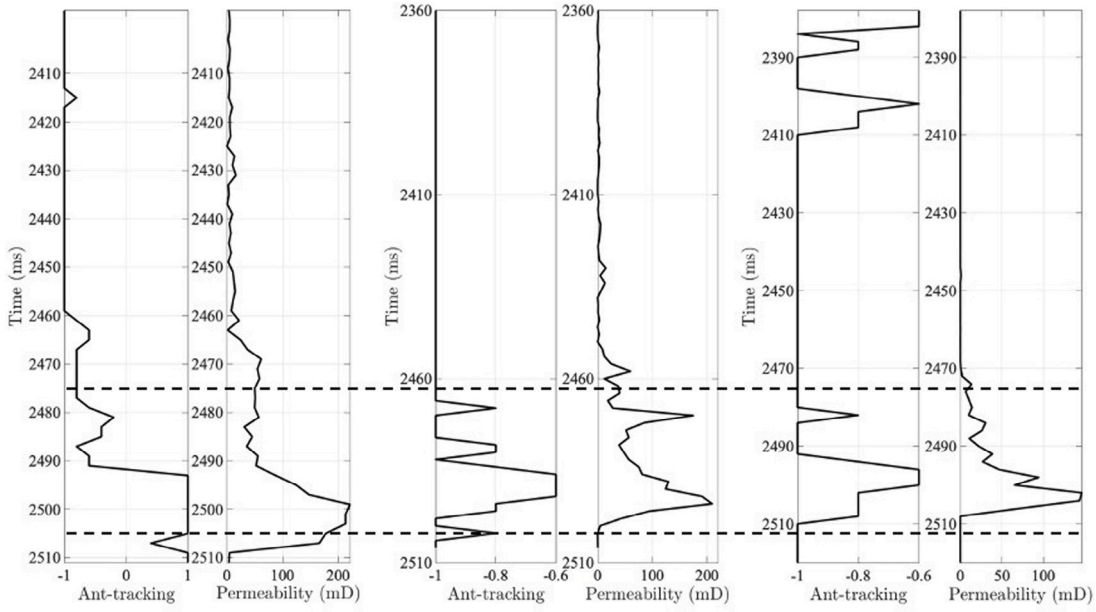

Fig. 16. Comparison between the ant-tracking seismic attribute at the well location and well-log data.

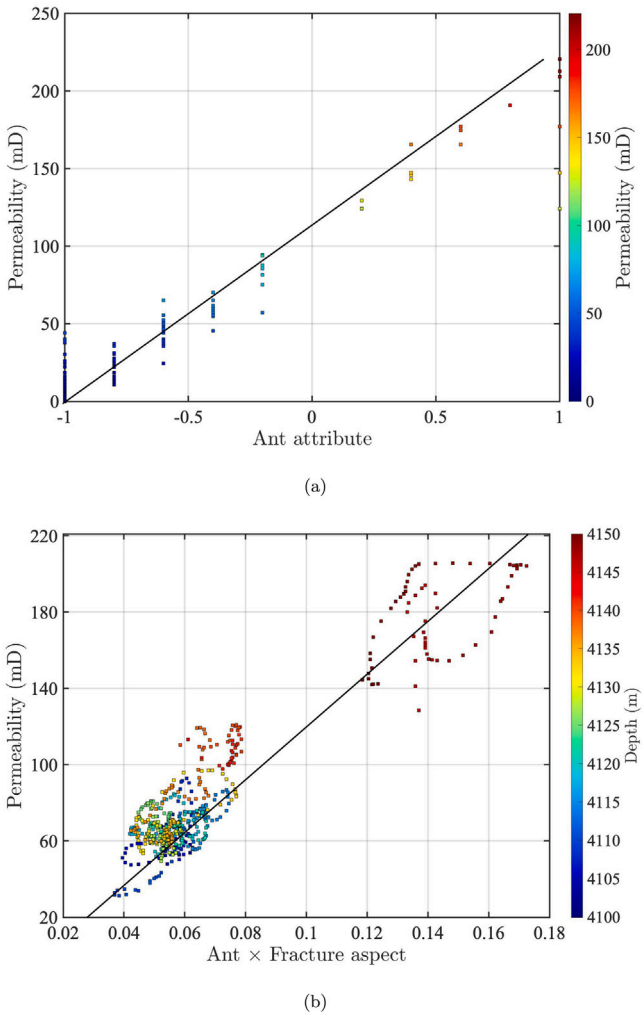

Fig. 17. Cross-plot analysis between the seismic attribute at the well location and permeability from the well-log.

whereas the aspect ratio the potential for flow and storage, and water saturation the possible presence of hydrocarbons. In fact, high fracture density and aspect ratio and low water saturation indicates the presence of shale gas.

Permeability can be obtained based on a cross-plot analysis by using the inversion results. In general, permeability is directly related to the pore structure. Macroscopic tectonic faults or fractures, as well as mesoscopic fractures, have significant effects on permeability. The ant-tracking technique is used to identify the fracture development (Randen et al., 2001; Pedersen et al., 2002, 2003; Zhao et al., 2018). Fig. 15 shows an ant-tracking map of fractures. The specific implement of ant tracking is shown in Appendix B.

The seismic properties (ant-tracking attribute) and petrophysical properties (permeability) at the borehole location are extracted and compared to the well-log data, and here we display the curves of the three most representative wells (Wells A, B, and C in Fig. 8) in the research area, as shown in Fig. 16. The seismic well tie is used to establish a mapping between depth-domain well-log data and time-domain seismic data. By comparison, it is shown that the ant-tracking-based seismic attribute is consistency with permeability. It could be possible to establish a permeability map with petrophysical analysis or deep learning methods (Yang et al., 2022). It can be found that the permeability profile corresponds well to the fracture aspect ratio and there is a linear relationship between the ant-tracking attributes and permeability through cross-plot analysis, as shown in Fig. 17a. Then, we multiply the normalized ant-tracking properties (in the range from 0 to 1) with the fracture aspect ratio and obtain a linear relationship between this product and permeability (Zhao et al., 2018) (see Fig. 17b). The best-fit linear relation is

$$\text{Permeability} = 1376.42 \cdot \left(\frac{\text{NANT} + 1}{2} \cdot \chi \right) - 476.58. \tag{29}$$

where NANT denotes the ant-tracking attribute. The permeability distribution is given in Fig. 18.

In Fig. 19 we compare the results of the inversion with logs from well A. The log profiles have been smoothed (blue solid lines), and it can be found that there is an acceptable agreement, indicating the good performance of the methodology.

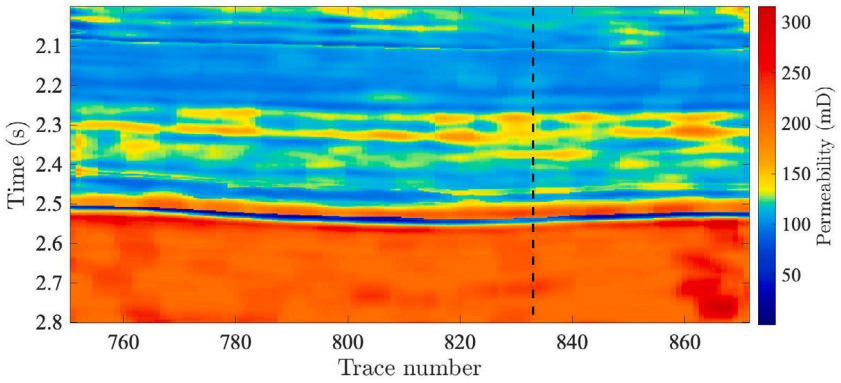

Fig. 18. Estimated permeability by using the results of the proposed AVAZ inversion.

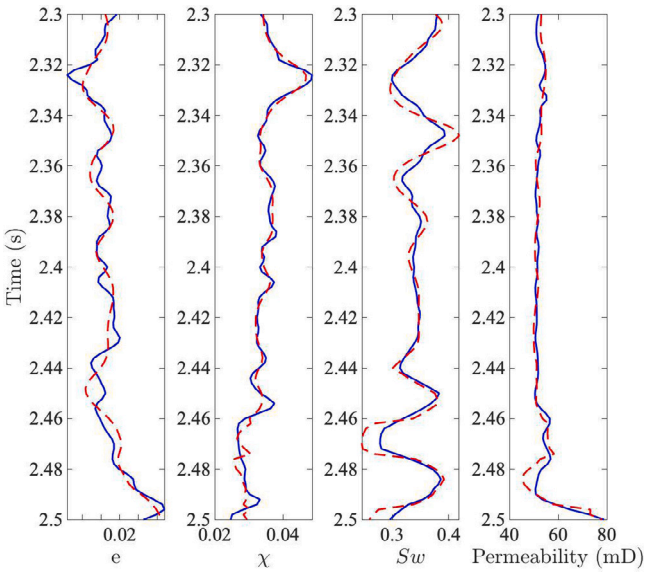

Fig. 19. Comparison between the smoothed well-log profiles (blue solid lines) and inverted fracture density, aspect ratio, water saturation and estimated permeability (red dashed lines).

6. Conclusions

Existing methods to estimate fracture properties in shale-gas reservoirs are oriented to obtain elasticity constants, anisotropic coefficients or fracture weakness, instead of fracture parameters. We implement an approach, where the fracture weaknesses are decoupled on the basis of the linear-slip model and the Wood equation, in terms of fracture density, aspect ratio and fluid saturation. Then, we propose a rock-physics-based AVAZ inversion method to retrieve the fracture geometrical properties, i.e., fracture density and aspect ratio from azimuthal seismic data. Furthermore, we estimate the permeability from the fracture aspect ratio spatial variability. The proposed method aims at improving the reliability of reservoir fracture properties prediction, which is important in geophysical exploration.

CRediT authorship contribution statement

Guangtan Huang: Methodology, Writing – original draft. **Jing Ba:** Conceptualization, Supervision, Review and editing. **Davide Gei:** Review and editing. **José M. Carcione:** Reviewing and editing.

Data availability

Data will be made available on request.

Acknowledgments

This work is supported by the Natural Science Foundation of Hubei (2022CFB862), National Natural Science Foundation of China (42004111), Jiangsu Innovation and Entrepreneurship Plan, and Jiangsu Province Science Fund for Distinguished Young Scholars.

Appendix A

A.1. Slowness and wave vectors

The polarization vectors of the incident and reflected P waves in TI media are

$$\mathbf{t} = [\sin\theta\cos\phi, \sin\theta\sin\phi, \cos\theta],$$
$$\mathbf{t}' = [-\sin\theta\cos\phi, -\sin\theta\sin\phi, \cos\theta], \tag{30}$$

respectively, and the corresponding slowness vectors are

$$\mathbf{p} = \frac{1}{\alpha_b}[\sin\theta\cos\phi, \sin\theta\sin\phi, \cos\theta],$$
$$\mathbf{p}' = \frac{1}{\alpha_b}[-\sin\theta\cos\phi, -\sin\theta\sin\phi, \cos\theta]. \tag{31}$$

Moreover,

$$\xi = t_i t_i'|_{r=r_0} = \cos 2\theta, \tag{32}$$

where r is the source–receiver distance, r_0 represents the stationary point, and

$$\eta_{IJ} = t_i' p_j' t_k p_l|_{r=r_0}, (i,j,k,l = 1,2,\ldots,6) \tag{33}$$

are the components of matrix **E** (See Box I)

We obtain R_{PP}^{ani} by substituting Eqs. (14), (33) and (34) into (13).

Appendix B

B.1. Ant tracking algorithm

The workflow of the ant-tracking method can be seen in Fig. 20, and the details is:

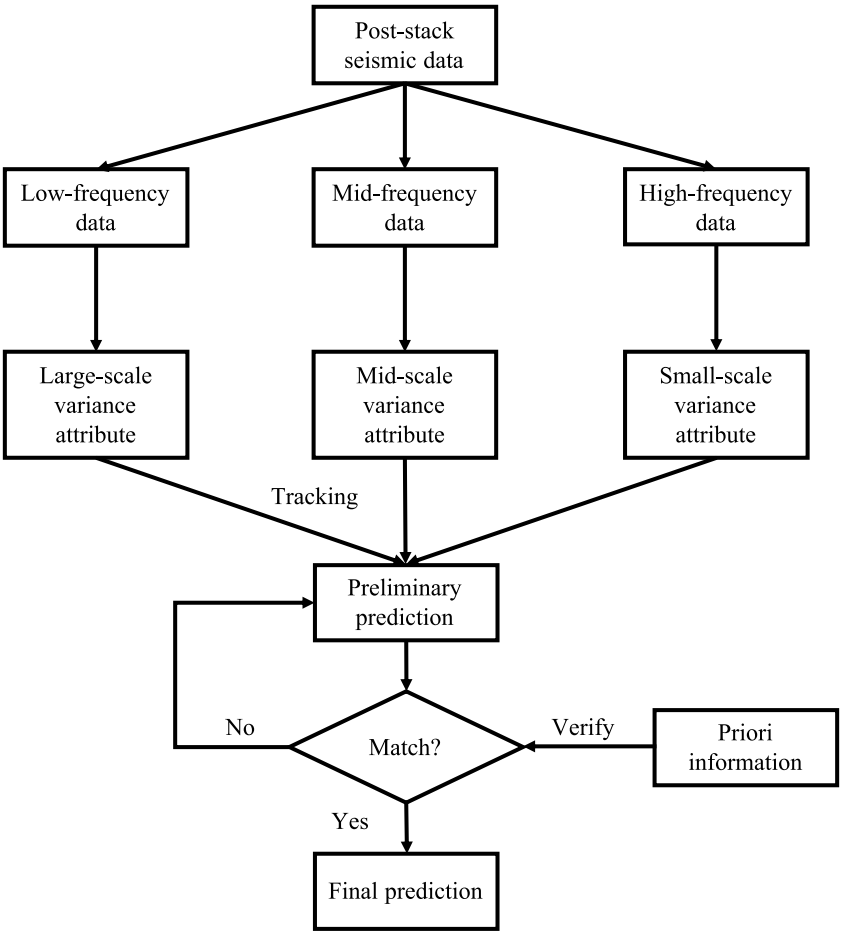

Fig. 20. Workflow of the ant-tracking algorithm.

$$\mathbf{E} = \frac{1}{\alpha_b^2}\begin{bmatrix} \sin^4\theta\cos^4\phi & \sin^4\theta\sin^2\phi\cos^2\phi & \sin^2\theta\cos^2\theta\cos^2\phi & 2\sin^3\theta\cos\theta\sin\phi\cos^2\phi & -2\sin^3\theta\cos\phi\cos^3\phi & 2\sin^4\theta\sin\phi\cos^3\phi \\ \sin^4\theta\sin^2\theta\cos^2\phi & \sin^4\theta\sin^4\phi & \sin^2\theta\cos^2\theta\sin^2\phi & -2\sin^3\theta\cos\theta\sin^3\phi & -2\sin^3\theta\cos\theta\sin^2\phi\cos\phi & 2\sin^4\theta\sin^3\phi\cos\phi \\ \sin^2\theta\cos^2\theta\cos^2\phi & \sin^2\theta\cos^2\theta\sin^2\phi & \cos^4\theta & 2\sin\theta\cos^3\theta\sin\phi & -2\sin\theta\cos^3\theta\cos\phi & 2\sin^2\theta\cos^2\theta\sin\phi\cos\phi \\ -2\sin^3\theta\cos\theta\sin\phi\cos^2\phi & 2\sin^3\theta\cos\theta\sin^3\phi & -2\sin\theta\cos^3\theta\sin\phi & -4\sin^2\theta\cos^2\theta\sin^2\phi & -4\sin^2\theta\cos^2\theta\sin\phi\cos\phi & -4\sin^3\theta\cos\theta\sin^2\phi\cos\phi \\ 2\sin^3\theta\cos\theta\cos^3\phi & 2\sin^3\theta\cos\theta\sin^2\phi\cos\phi & 2\sin\theta\cos^3\theta\cos\phi & -4\sin^2\theta\cos^2\theta\sin\phi\cos\phi & -4\sin^2\theta\cos^2\theta\cos^2\phi & -4\sin^3\theta\cos\theta\sin\phi\cos^2\phi \\ 2\sin^4\theta\sin\phi\cos^3\phi & 2\sin^4\theta\sin^3\phi\cos\phi & 2\sin^2\theta\cos^2\theta\sin\phi\cos\phi & 4\sin^3\theta\cos\theta\sin^2\phi\cos\phi & 4\sin^3\theta\cos\theta\sin\phi\cos^2\phi & 4\sin^4\theta\sin^2\phi\cos^2\phi \end{bmatrix}. \tag{34}$$

Box I.

(1): Conventional fracture identification property extraction

The ant tracking algorithm is a reprocessing method that implements on the conventional fracture identification body properties, such as variance attribute, curvature property, etc. Such properties detect the discontinuity of seismic event. Here we extract the variance attributes (Bahorich and Farmer, 1995; Marfurt et al., 1998; Gersztenkorn and Marfurt, 1999) from the post-stack seismic data as an input data.

(2): Determining the number of ants, initial positions and movement direction.

The variance attributes are divided into a number of cells with an ant each cell. Thus, the amount of ant is

$$M_{ant} = \mathrm{INT}\left(\frac{N_x \times N_y \times N_z}{d_x \times d_y \times d_z}\right) \tag{35}$$

where INT is the integer algorithm, N_x, N_y, and N_z are the numbers of lines, CDPs, and time samples, d_x, d_y, and d_z are the size of cells. Then, we normalize the data within each cell and calculate the probability of each point according to

$$P_i = \frac{1 - C_i}{\sum_{j=1}^{N_c}\left(1 - C_j\right)}, \tag{36}$$

where N_c is the number of samples in each cell. The initial position of the ant tracking corresponds to the point with the highest probability. Then, we calculate the directional gradient covariance matrix, which is given by

$$\mathbf{V} = \begin{bmatrix} G_{xx} & G_{xy} & G_{xz} \\ G_{yx} & G_{yy} & G_{zz} \\ G_{zx} & G_{zy} & G_{zz} \end{bmatrix} = \begin{bmatrix} G_x^2 & G_xG_y & G_xG_z \\ G_yG_x & G_y^2 & G_yG_z \\ G_zG_x & G_zG_y & G_z^2 \end{bmatrix} \tag{37}$$

where G denotes the gradient along each direction. The eigenvalue decomposition of **V** yields three eigenvalues, of which the three eigenvectors v_1, v_2, v_3 corresponding to the largest eigenvalue ϵ_1 can be adopted to calculate the tracking direction.

(3): Automatically tracking and update preliminary predictions

Start tracking after setting the parameters. Preliminary predictions are updated when a trace has been completed.

(4): Verify and output final fracture prediction results

Some priori information is used to verify the results of the ant tracking fracture detection based on body curvature. If they match each other, output the fracture prediction results. Otherwise, adjust the parameters of the ant tracking algorithm to recalculate until the two match.

References

Alemie, W., Sacchi, M.D., 2011. High-resolution three-term AVO inversion by means of a trivariate Cauchy probability distribution. Geophysics 76 (3), R43–R55.

Bachrach, R., Sengupta, M., Salama, A., Miller, P., 2009. Reconstruction of the layer anisotropic elastic parameters and high-resolution fracture characterization from P-wave data: a case study using seismic inversion and Bayesian rock physics parameter estimation. Geophys. Prospect. 57 (2), 253–262.

Bahorich, M., Farmer, S., 1995. 3-D seismic discontinuity for faults and stratigraphic features: The coherence cube. Lead. Edge 14 (10), 1053–1058.

Bakulin, A., Grechka, V., Tsvankin, I., 2000a. Estimation of fracture parameters from reflection seismic data|part I: HTI model due to a single fracture set. Geophysics 65 (6), 1788–1802.

Bakulin, A., Grechka, V., Tsvankin, I., 2000b. Estimation of fracture parameters from reflection seismic data-part II: Fractured models with orthorhombic symmetry. Geophysics 65 (6), 1803–1817.

Carcione, J.M., Gurevich, B., Santos, J.E., Picotti, S., 2013. Angular and frequency dependent wave velocity and attenuation in fractured porous media. Pure Appl. Geophys. 170, 1673–1683.

Carcione, J.M., Picotti, S., 2012. Reflection and transmission coefficients of a fracture in transversely isotropic media. Studia Geophys. Geodaetica 56, 307–322.

Carcione, J.M., Picotti, S., Santos, J.E., 2012. Numerical experiments of fracture induced velocity and attenuation anisotropy. Geophys. J. Int. 191, 1179–1191.

Chen, H., Ji, Y., Innanen, K.A., 2018. Estimation of modified fluid factor and dry fracture weaknesses using azimuthal elastic impedance. Geophysics 83 (1), WA73–WA88.

Chen, H., Pan, X., Ji, Y., Zhang, G., 2017. Bayesian Markov chain Monte Carlo inversion for weak anisotropy parameters and fracture weaknesses using azimuthal elastic impedance. Geophys. J. Int. 210 (2), 801–818.

Chen, J., Wang, L., Wang, C., et al., 2021. Automatic fracture optimization for shale gas reservoirs based on gradient descent method and reservoir simulation. Adv. Geo-Energy Res. 5 (2), 191–201.

Chen, H., Yin, X., Gao, J., Liu, B., Zhang, G., 2015. Seismic inversion for underground fractures detection based on effective anisotropy and fluid substitution. Sci. China Earth Sci. 58 (5), 805–814.

Chen, H., Yin, X., Gao, C., Zhang, G., Chen, J., 2014. AVAZ inversion for fluid factor based on fractured anisotropic rock physics theory. Chinese J. Geophys. 57 (3), 968–978.

Crampin, S., 1984. Effective anisotropic elastic constants for wave propagation through cracked solids. Geophys. J. Int. 76 (1), 135–145.

Domenico, S.N., 1976. Effect of brine-gas mixture on velocity in an unconsolidated sand reservoir. Geophysics 41 (5), 882–894.

Gersztenkorn, A., Marfurt, K.J., 1999. Eigen structure based coherence computations as an aid to 3-D structural and stratigraphic mapping. Geophysics 64 (5), 1468, 1479.

Hsu, C.J., Schoenberg, M., 1993. Elastic waves through a simulated fractured medium. Geophysics 58 (7), 964–977.

Huang, G., Chen, X., Luo, C., et al., 2020. Geological structure-guided initial model building for prestack AVO/AVA inversion. IEEE Trans. Geosci. Remote Sens. 59 (2), 1784–1793.

Hudson, J.A., 1981. Wave speeds and attenuation of elastic waves in material containing cracks. Geophys. J. Int. 64 (1), 133–150.

Jin, S., Stovas, A., 2020. S-wave in 2d acoustic transversely isotropic media with a tilted symmetry axis. Geophys. Prospect. 68 (2), 483–500.

Li, H., Yu, F., Wang, M., et al., 2022. Quantitative prediction of structural fractures in the Paleocene lower Wenchang formation reservoir of the Lufeng Depression. Adv. Geo-Energy Res. 6 (5), 375–387.

Marfurt, K.J., Kirlin, R.L., Farmer, S.L., et al., 1998. 3-D seismic attributes using a semblance based coherency algorithm. Geophysics 63 (4), 1150–1165.

Oh, J.W., Alkhalifah, T., 2016. The scattering potential of partial derivative wave-fields in 3-d elastic orthorhombic media: an inversion prospective. Geophys. J. Int. 206 (3), 1740–1760.

Pan, X., Li, L., Zhou, S., Zhang, G., Liu, J., 2021. Azimuthal amplitude variation with offset parameterization and inversion for fracture weaknesses in tilted transversely isotropic media. Geophysics 86 (1), C1–C18.

Pan, X., Zhang, G., Yin, X., 2018. Azimuthally pre-stack seismic inversion for orthorhombic anisotropy driven by rock physics. Sci. China Earth Sci. 61 (4), 425–440.

Pan, X., Zhang, G., Yin, X., 2019a. Amplitude variation with offset and azimuth inversion for fluid indicator and fracture weaknesses in an oil-bearing fractured reservoir. Geophysics 84 (3), N41–N53.

Pan, X., Zhang, G., Yin, X., 2019b. Linearized amplitude variation with offset and azimuth and anisotropic poroelasticity. Geophys. Prospect. 67 (7), 1882–1897.

Pedersen, S.I., Randen, T., Sønneland, L., Steen, Ø., 2002. Automatic fault extraction using artificial ants. In: 72nd Annual International Meeting SEG Technical Program Expanded Abstracts. Society of Exploration Geophysicists, pp. 2452–2456.

Pedersen, S.I., Skov, T., Hetlelid, A., Fayemendy, P., Ramden, T., Sonneland, L., 2003. New paradigm of fault interpretation. In: 73rd Annual International meeting SEG Technical Program Expanded Abstracts. Society of Exploration Geophysicists, pp. 350–353.

Qin, Z., Wen, X., Zhou, D., et al., 2021. Inversion method of elastic and fracture parameters of shale reservoir with a set of inclined fractures. IEEE Trans. Geosci. Remote Sens. http://dx.doi.org/10.1109/TGRS.2021.3138750.

Randen, T., Pedersen, S.I., Snneland, L., 2001. Automatic detection and extraction of faults from three-dimensional seismic data. In: 71st Annual International meeting SEG Technical Program Expanded Abstracts. Society of Exploration Geophysicists, pp. 551–555.

Rüger, A., 1997. P-wave reflection coefficients for transversely isotropic models with vertical and horizontal axis of symmetry. Geophysics 62, 713–722.

Rüger, A., 1998. Variation of P-wave reflectivity with offset and azimuth in anisotropic media. Geophysics 63, 935–947.

Rüger, A., 2002. Reflection coefficients and azimuthal AVO analysis in anisotropic media. In: 72nd Annual International meeting SEG Technical Program Expanded Abstracts. Society of Exploration Geophysicists, pp. 551–555.

Schoenberg, M., Protazio, J., 1990. Zoeppritz rationalized, and generalized to anisotropic media. J. Acoust. Soc. Am. 88 (1), S46.

Schoenberg, M., Sayers, C.M., 1995. Seismic anisotropy of fractured rock. Geophysics 60 (1), 204–211.

Sen, M.K., Roy, I.G., 2003. Computation of differential seismograms and iteration adaptive regularization in prestack waveform inversion. Geophysics 68 (6), 2026–2039.

Shaw, R.K., Sen, M.K., 2004. Born integral, stationary phase and linearized reflection coefficients in weak anisotropic media. Geophys. J. Int. 158 (1), 225–238.

Shaw, R.K., Sen, M.K., 2006. Use of AVOA data to estimate fluid indicator in a vertically fractured medium. Geophysics 71 (3), C15–C24.

Thomsen, L., 1986. Weak elastic anisotropy. Geophysics 51 (10), 1954–1966.

Xue, J., Gu, H., Cai, C., 2017. Model-based amplitude versus offset and azimuth inversion for estimating fracture parameters and fluid content. Geophysics 82 (2), M1–M17.

Yang, C., Liu, J., 2021. Petroleum rock mechanics: An area worthy of focus in geo-energy research. Adv. Geo-Energy Res. 5 (4), 351–352.

Yang, L., Wang, S., Chen, X., et al., 2022. High-fidelity permeability and porosity prediction using deep learning with the self-attention mechanism. IEEE Trans. Neural Netw. Learn. Syst. http://dx.doi.org/10.1109/TNNLS.2022.3157765.

Zhao, W., Sun, D., Zhang, T., et al., 2018. Application of improved ant-tracking method in carbonate-fracture reservoir. In: 88th Annual International Meeting SEG Technical Program Expanded Abstracts. Society of Exploration Geophysicists, pp. 1633–1638.